

Ice-nucleation properties of aluminum surfaces

*Carlotta E. A. Blamey-Beccaria, Michael A. Parkes, Jinjie Li and Christoph G. Salzmann**

Department of Chemistry, University College London, 20 Gordon Street, London WC1H 0AJ, United Kingdom.

Corresponding Author

Prof. Christoph G. Salzmann
Department of Chemistry
University College London
London WC1H 0AJ, UK
Tel.: +44 7679 8864
Email: c.salzmann@ucl.ac.uk

Abstract

The nucleation of ice from supercooled water droplets plays a critical role across various technological sectors including aviation, power transmission, shipping and space flight. Despite its importance, the fundamental mechanisms of water freezing on surfaces remain poorly understood. In this study, we investigate the freezing behavior of supercooled droplets on several aluminum alloys (1050, 5083, 5251, 6060 and 6082) using our custom-designed IceBox instrument. Our findings show that all aluminum surfaces exhibit moderate ice-nucleating capabilities. High levels of surface oxidation and magnesium content lead to higher average ice-nucleation temperatures, and rough surfaces generally promote ice formation more effectively than polished ones. An exception is the freshly polished 1050 alloy, the softest and purest aluminum examined, where micrometer-scale “pit” features appear to initiate ice nucleation. After surface aging, the 5251 alloy displays the highest ice-nucleating ability, while the 6082 alloy shows the lowest. Overall, our results highlight the importance of considering the interplay between surface roughness, specific defects and alloy composition when aiming to reduce ice formation on aluminum surfaces.

Introduction

Water can remain liquid well below its freezing point for extended periods of time. Under rapid cooling conditions, freezing temperatures as low as $-46\text{ }^{\circ}\text{C}$ have been reported.¹ Even at such low temperatures, ice nucleation may not occur homogeneously but can instead be triggered by the surfaces of the water droplets.² At higher temperatures, ice typically nucleates heterogeneously at the interface between liquid water and solid particles or surfaces. For effective nucleation to occur, the ice-nucleating surface must be large enough to support the formation of a critical ice nucleus.³⁻⁵ Notable examples of efficient ice nucleators include silver halides⁶⁻⁸ and biological particles originating from *Pseudomonas syringae* bacteria.⁹⁻¹² Heterogeneous ice nucleation plays a critical role in diverse fields, including climate science, biology, aviation, space flight, food industry and the cryopreservation biological materials.¹³⁻¹⁹

Computational studies have played a crucial role in uncovering the molecular-scale mechanisms underlying ice nucleation.^{12, 20-23} Experimentally, one of the main challenges in studying ice nucleation lies in the fact that only a few active sites on a surface may trigger nucleation, and these sites often have structures that do not necessarily reflect the bulk properties of the material.²⁴⁻²⁷ Despite recent advances, the fundamental question of what drives water to freeze remains incompletely understood.²⁸

Aluminum surfaces are widely used across numerous industries, including aviation, automotive, construction, shipping and space flight. Wrought aluminum alloys are commonly identified by a four-digit code, where the first digit denotes the principal alloying element, except in the case of the 1xxx series, which defines pure aluminum with a minimum purity of 99%.²⁹ The second digit (if not zero) indicates a variation of the original alloy, while the last two digits specify the particular alloy within that series.

When exposed to air, aluminum reacts rapidly with oxygen to form a surface layer of aluminum oxide.^{30, 31} This process begins with the formation of an amorphous precursor, eventually yielding a $\gamma\text{-Al}_2\text{O}_3$ layer.³² In the context of ice nucleation, nine different aluminum oxides have been evaluated using immersion freezing experiments. Among them, corundum (α -alumina) was identified as the most effective ice-nucleating Al_2O_3 material.³³ Computational studies attribute this to the favorable lattice match between the hexagonal structure of α -alumina and that of ice.³⁴ Investigations into the pH dependence of ice nucleation showed that the α -alumina (0001) surface exhibited the highest freezing temperatures at neutral pH.³⁵ Classical

molecular dynamics simulations suggest this is due to the presence of mono-protonated OH groups at neutral pH, which are particularly effective at promoting ice-like structuring of the water at the interface.³⁶ On the other hand, the freezing temperatures of supercooled KCl solutions on 1050 aluminum surfaces were found to be only minimally influenced by pH.³⁷ Alumina nanoparticles have also been employed as model systems for atmospheric mineral dust.³⁸ Additionally, aluminum surfaces are widely used as substrates for the development of icephobic coatings.³⁹⁻⁴¹

In this study, we examine the ice-nucleation properties of a selection of commercially available aluminum alloys. These include nearly pure aluminum (1050), aluminum primarily alloyed with magnesium (5083 and 5251), and alloys from the 6xxx series, where aluminum is combined with both magnesium and silicon (6060 and 6082). To perform the ice-nucleation experiments, we designed a custom instrument, the IceBox, to monitor the supercooling and freezing of 7×7 arrays of water droplets as the aluminum surfaces are cooled. Both rough and polished surfaces are characterized using high-resolution optical microscopy with the digital depth composition function, providing detailed surface roughness parameters. Elemental surface compositions are determined with laser-induced breakdown spectroscopy. Finally, the effects of surface roughness, chemical composition and aging are correlated with the observed ice-nucleation behaviors.

Experimental section

Aluminum samples

Aluminum sheets with a thickness of 6 mm were obtained from commercial suppliers including the 1050, 5083, 5251, 6060 and 6082 alloys. The nominal elemental compositions of these alloys are provided in Table 1.²⁹ From each sheet, 40×40 mm squares were cut, and a 3 mm-diameter hole with a depth of 25 mm was drilled near one of the edges to accommodate a temperature sensor.

Table 1. Elemental compositions of the aluminum alloys used in this study in atom percentage.²⁹

Alloys	1050	5083	5251	6060	6082
Al	99.5	balance	balance	balance	balance
Si	0.25	0.4-0.7	0.4	0.3-0.6	0.7-1.3
Fe	0.4	0.4	0.5	0.1-0.3	0.5
Cu	0.05	0.1	0.15	0.1	0.1
Mn	0.05	0.4-1.0	0.1-0.5	0.1	0.4-1.0
Mg	0.05	4.0-4.9	1.7-2.4	0.35-0.6	0.6-1.2
Cr	0	0.05-0.25	0.15	0.05	0.25
Zn	0.05	0.25	0.15	0.15	0.2
V	0.05	0	0	0	0
Ti	0.03	0.15	0.15	0.1	0.1
trace elements	0.03	0.15	0.15	0.15	0.15

Preparation of the aluminum surfaces

To prepare rough surfaces, the aluminum sheets were sanded with a grade P100 sandpaper. The surfaces were then rinsed with isopropanol to remove any contaminants. Isopropanol was chosen as a cleaning solvent due to its well-known ability to evaporate quickly at room temperature without leaving residues.

To achieve smooth surfaces, the aluminum samples were initially sanded with P100 sandpaper, followed by P400 sandpaper, to remove any visible deep scratches, and then P800 sandpaper. After this, the surfaces were cleaned with Cif cream cleaner, rinsed with water, and sanded using P1000 and P4000 sandpapers. Finally, the surfaces were polished using a soft cloth and Brasso metal polish, and rinsed with isopropanol to remove residual polish.

Optical digital microscopy

A Keyence VHX-970F optical microscope was used for determining the surface roughness of the different samples using 5000-fold magnification with a VH-Z500T objective and the fine-depth composition function of the microscope software. At this magnification, areas of 2913 μm^2 were captured. Out-of-focus distances were defined manually well above and below the surfaces, and a stack of 200 images was then automatically collected between the two extremes. The software of the microscope was then used to reconstruct a 3D model of the surface and to calculate various characteristics of the surface roughness. Measurements were taken at ten random locations across each of the surfaces including the rough and polished surfaces.

Laser-induced breakdown spectroscopy (LIBS)

Approximately two months after the preparation of the polished surfaces, the chemical surface compositions were determined using a laser-induced breakdown spectroscopy (LIBS) module of a Keyence VHX-7000 microscope.

Ice nucleation experiments

The ice nucleation experiments were conducted with our IceBox instrument which was designed and built by us for this study. A schematic cross-section of its main unit is shown in Figure 1(a) and a top-view photographic image in Figure 1(b). The IceBox consists of a (1) cylindrical housing which was 3D-printed using white tough PLA (150 mm diameter, 130 mm height). A (2) lid with an opening for a (3) USB document camera and three holders for (4) white LED backlight modules (Pimoroni, 3 V, 38.7 mm × 11.9 mm) was 3D printed using black tough PLA for the inside and white PLA for the outside surfaces. The LED backlight modules were oriented so that the light reflected from the white internal walls of the housing and operated with a power supply. At the bottom of the IceBox, a (5) copper heat exchanger (Laird Technologies Liquid Heat Exchanger, 12.7 × 57 × 51 mm) was firmly attached to a small stage with two M3 bolts and nuts. A (6) circular floor was CNC-milled from a 3 mm thick Perspex sheet containing a rectangular opening with steps so that the Perspex sheet can rest on the edges of the heat exchanger while still exposing most of its upper copper surface. Several 3 mm diameter holes were drilled into the Perspex sheet surrounding the heat exchanger. Once installed, the small gap between the Perspex floor and the housing was filled with silicone. A (7) Peltier element (RS Components, 82.1 W, 8.4 A, 15.7 V, 40 × 40 mm) was then firmly attached to the heat exchanger using small amounts of heat-conducting paste and ensuring that its hot side was in contact with the heat exchanger. One of the various (8) aluminum squares was then attached to the upper side of the Peltier element again using small amounts of heat-conducting paste. A (9) Pt100 temperature sensor (RS PRO Pt100 RTD probe, 2.8 mm diameter, 25 mm long, Class A) in 4-wire configuration was inserted sideways into the hole of the aluminum sample using heat-conducting paste to achieve good thermal contact. On top of the aluminum surface, a (10) 2 mm high, black 3D-printed PLA grid was placed with 7×7 compartments. Into the compartments, an (11) array of 49 Milli-Q water droplets with volumes of 1 μL was pipetted. The purpose of the grid was to prevent any potential interactions between

neighboring droplets of water either through Ostwald ripening when liquid or through ejecta from freezing droplets causing the nucleation of neighboring droplets.^{42, 43}

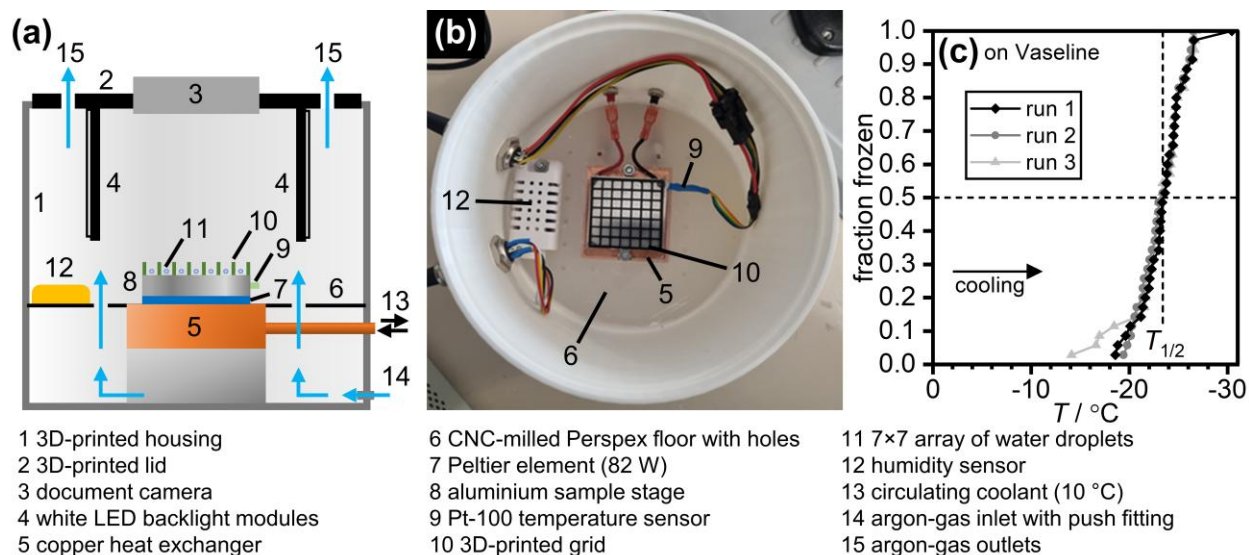


Figure 1. (double column) IceBox instrument for measuring the ice-nucleation abilities of aluminum surfaces. (a) Schematic cross-section of the IceBox and (b) top-view photographic image with the lid removed. The various components are labeled with numbers and described in the legend. (c) Fraction-frozen curves obtained from three independent cooling experiments at 1 °C min⁻¹ with 49 water droplets (1 μL) placed on Vaseline-coated aluminum surfaces.

The IceBox also hosts a (12) humidity sensor (Adafruit, SHT30, enclosed shell) attached to the Perspex floor. The (5) heat exchanger was connected to (13) coolant from a Julabo F1000 thermoregulation system operating at 10 °C. Using a (14) push fitting at the bottom of the IceBox, its internal volume was purged with dry argon gas. An argon flow rate of 0.8 L min⁻¹ was used during the ice nucleation experiments.

The Perspex floor at the height level just below the array of water droplets ensured that the lower compartment of the IceBox was always fully filled with dry argon even when the top lid was taken off for pipetting the water droplets onto the aluminum surfaces. This meant that the humidity at the height level of the water droplets could be reduced very quickly. The condensation of frost due to high humidity levels needed to be strictly avoided since this would lead to immediate ice nucleation of the supercooled water droplets.⁴⁴ Several (15) holes in the top lid ensured a constant flow of dry argon gas through the IceBox from the bottom towards the top.

Various electronic components were housed in a separate box. These included a microcontroller (Adafruit Feather 32u4 Basic Proto) connected to an Adafruit Pt100 RTD temperature sensor amplifier. The humidity sensor was connected directly to the microcontroller whereas the four wires from the Pt100 sensor inside the main unit were connected to the amplifier. The code for the microcontroller was written so that it interrogates the temperature of the Pt100 sensor and the humidity, and, for convenience, both values were displayed at the front of the electronics box using two LED displays. The microcontroller was also connected to a Windows computer via its USB port.

On the computer, a LabView program was designed which requested both the temperature and humidity from the microcontroller. Within the program, a cooling ramp could be defined in terms of start and end temperature as well as cooling rate. The USB port of the computer was connected to the RS232 port of a power supply (RS PRO Digital Bench Power Supply, 20 V DC, 10 A, 200 W) using an USB to RS232 converter, and the terminals of the power supply were connected to the Peltier element inside the IceBox. Using a PID algorithm, the LabView program could then set the voltage of the Peltier element so that the defined cooling ramp was followed. The temperatures during a typical cooling experiment from +5 to $-30\text{ }^{\circ}\text{C}$ at $1\text{ }^{\circ}\text{C min}^{-1}$ are shown in Figure S1.

Additionally, the LabView program takes images of the array of droplets on the sample stage using the USB document camera at one second intervals during cooling. The current temperature was written at the top left-hand corner of every image. The polished aluminum surfaces were highly reflective which represented a challenge when trying to capture images from directly above. The glare was minimized by bouncing the LED light off the white wall of the container and by using black PLA for the underside of the top lid. The freezing of the water droplets goes along with a visible change in the appearance of the droplets from transparent to white as well as changes in shape as shown in Figure S2. The temperatures of the various freezing events were determined by scrolling through the stack of recorded images. Whenever the freezing of a droplet was observed, the temperature was noted, and a small bead of blue tack was attached to the computer screen on top of the frozen droplet so that it was easier to keep an eye on the still liquid droplets. Once all droplets had frozen, the list of freezing temperatures was used to obtain fraction-frozen curves as they are shown, for example, in Figure 1(c).

The fraction-frozen curves in Figure 1(c) were obtained after applying a thin layer of Vaseline petroleum jelly onto an aluminum surfaces before pipetting the array of 1 μL Milli-Q water droplets. The hydrophobic Vaseline is known to exhibit poor ice-nucleation properties.⁴⁵⁻⁴⁷ There was consistent freezing behavior for the three experiments illustrating reproducibility. The average temperature at which half of the droplets were frozen, $T_{1/2}$, was -23.39 ± 0.18 $^{\circ}\text{C}$ for a cooling rate of 1 $^{\circ}\text{C min}^{-1}$. This $T_{1/2}$ value represents a baseline value for our setup. Any surface with ice-nucleation abilities is expected to show a more positive $T_{1/2}$ value.

To test the accuracy of the temperature measurements, arrays of frozen water droplets were heated from -30 to $+5$ $^{\circ}\text{C}$ at 0.5 $^{\circ}\text{C min}^{-1}$. Melting was observed consistently between 0.09 and 0.12 $^{\circ}\text{C}$ which was considered close enough to 0 $^{\circ}\text{C}$ so that no temperature corrections were performed. Furthermore, the melting was observed to be instantaneous across the entire surface illustrating that no thermal gradients are present across the sample stage.

All ice-nucleation experiments using the different aluminum surfaces were repeated at least three times. Fresh surfaces were prepared for every single experiment including for studies investigating the effects of surface aging. For aging the surfaces, the samples were stored in plastic boxes for up to 50 days to ensure that the surfaces stayed clean. Overall, 137 individual ice-nucleation experiments were performed for this study.

Results and Discussion

The as-prepared aluminum surfaces were first characterized with high-resolution optical microscopy. Representative images using 5000-fold magnification are shown in Figure 1. The polished surfaces showed flat areas with thin crisscrossing lines as well as a few dark patches. The polished 1050 surfaces displayed more of the dark defect features compared to the other polished surfaces. The 1050 alloy is the purest out of all the investigated alloys and hence also the softest.²⁹ As expected, the rough surfaces displayed significant and heavily overlapping scratches along random directions. No obvious visual differences could be seen comparing the different rough surfaces.

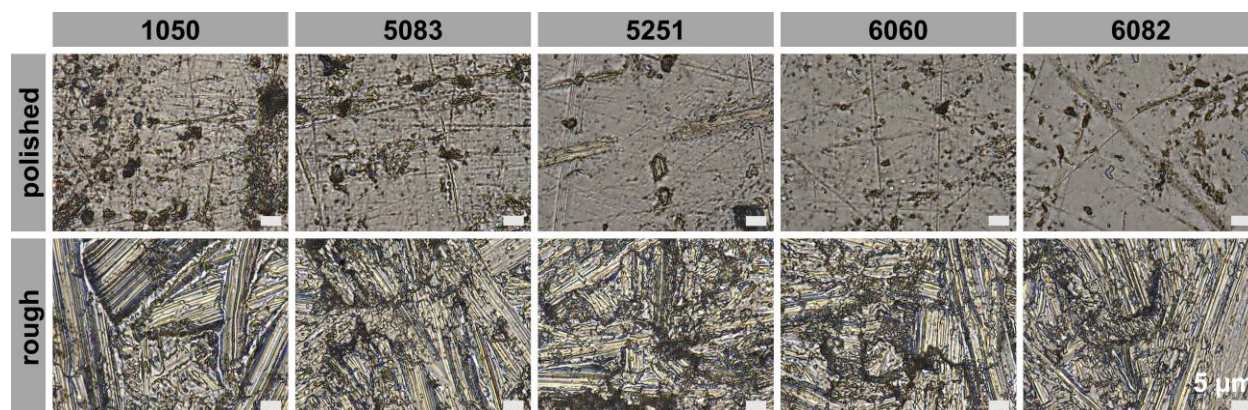


Figure 2. (double column) Optical-microscopy images of the as-prepared polished and rough aluminum surfaces recorded at 5000-fold magnification.

Stacks of 200 images were recorded as a function of height around the focal distance of a given location on one of the aluminum surfaces using the fine-depth composition function of our digital microscope. From such a set of images, the software of the microscope constructed three-dimensional representations of the surfaces. Figure 3 shows two examples of three-dimensional surface structures of (a) polished and (b) rough 1050 surfaces. As expected, the polished surface is much smoother compared to the rough surface. Also, using this type of three-dimensional analysis, it could be clarified that the dark features on the polished surfaces observed in Figure 2 are in fact “pits” with diameters around 5 μm and depths in the 1 to 2 μm range. One such pit is highlighted by the red arrow in Figure 3(a).

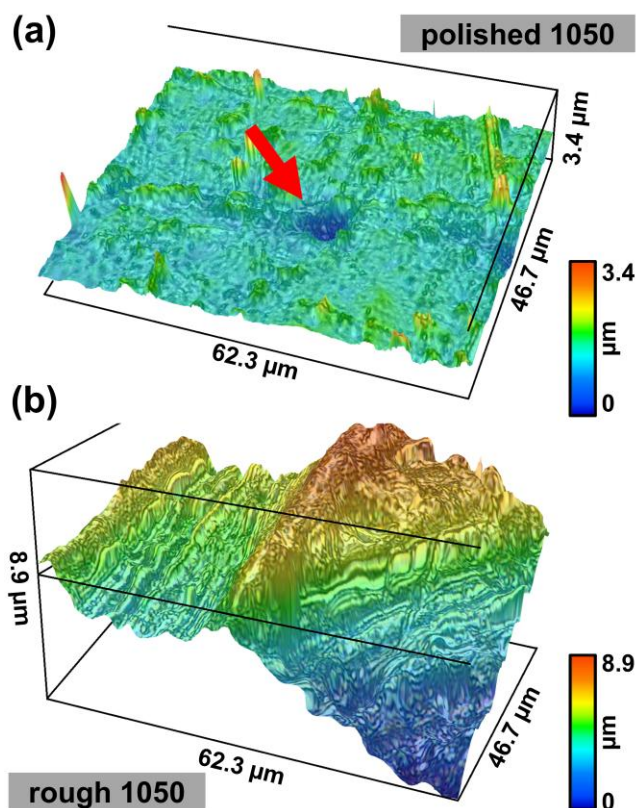


Figure 3. (single column) Three-dimensional surface structures of (a) polished and (b) rough 1050 aluminum surfaces. The height information is indicated by the rainbow-color gradient. The red arrow in (a) indicates the location of a “pit” feature.

From the three-dimensional information, various surface-roughness parameters were calculated. The most basic quantity is the surface roughness S_a , which reflects the average absolute height deviation from the mean surface plane. The average S_a values from ten different locations on the different aluminum substrates are shown in Figure 4(a). The polished surfaces show S_a values around $0.2\ \mu\text{m}$ with small spatial variations as indicated by the small vertical bars. The rough surfaces on the other hand showed larger S_a values around $1\ \mu\text{m}$ and pronounced spatial variations across a given surface.

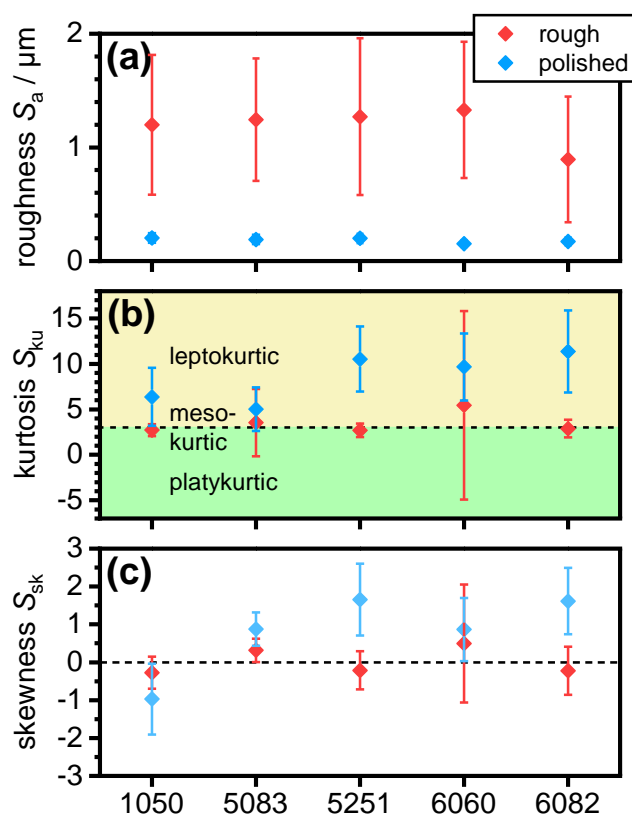


Figure 4. (single column) Average roughness parameters of the different rough and polished aluminum surfaces including (a) surface roughness S_a , (b) kurtosis S_{ku} and (c) skewness S_{sk} (see text for definitions). The vertical bars in this figure indicate the spatial variations across the surfaces in question.

The roughness analysis also gives the kurtosis of the height distributions, S_{ku} , as shown in Figure 4(b). The kurtosis is a measure for the sharpness of the height distribution where a value of 3 (mesokurtic) indicates a normal height distribution. S_{ku} values greater than 3 (leptokurtic) indicate more tall peaks and deep valleys whereas S_{ku} values less than 3 (platykurtic) imply fewer tall peaks and deep valleys than expected from a normal height distribution. On average, the rough surfaces can be classified as mesokurtic with $S_{ku} = 3$. This means that the average height distributions follow a normal distribution. The polished surfaces on the other hand are leptokurtic, *i.e.* $S_{ku} > 3$, which implies that the surfaces exhibit more tall and deep features than expected from a normal height distribution. This finding makes sense since our polishing procedure can be expected to remove smaller height variations preferentially.

The final parameter obtained from the roughness analysis is the skewness of the height distributions, S_{sk} . A skewness of zero means that the height distribution is symmetrical with respect to the mean plane. Positive and negative values indicate that the height distributions are skewed below or above the mean plane, respectively. As shown in Figure 4(c), the rough surfaces display average S_{sk} values around zero which means that the height distributions are symmetric with respect to the mean plane. This is expected for mesokurtic height distributions. For the polished surfaces, differences are observed between the 1050 alloy and the others. The 1050 alloy shows $S_{sk} < 0$ which means that the height distribution is skewed above the mean plane. This means that fewer peaks are present than deep surface features. This finding is consistent with the frequently observed pit structures on the polished 1050 surfaces. The other alloys show the opposite behavior for polished surfaces with $S_{sk} > 0$ indicating a prevalence of taller features.

In a next step, the ice-nucleation properties of the different as-prepared surfaces were investigated using our IceBox instrument. Fraction-frozen curves were obtained by cooling arrays of 49 one-microliter droplets of MilliQ water on the various aluminum surfaces at $1\text{ }^{\circ}\text{C min}^{-1}$. Figure 5 shows the combined fraction-frozen curves from at least three separate experiments for the polished and rough surfaces including the (a) 1050, (b) 5083, (c) 5251, (d) 6060 and (e) 6082 alloys. For comparison, the fraction-frozen curves of one-microliter water droplets on Vaseline are included in Figure 5. For all fraction-frozen curves, the temperatures at which half of the droplets were frozen, $T_{1/2}$, are indicated by dashed vertical lines. The shaded areas indicate the margins of error of the $T_{1/2}$ values.

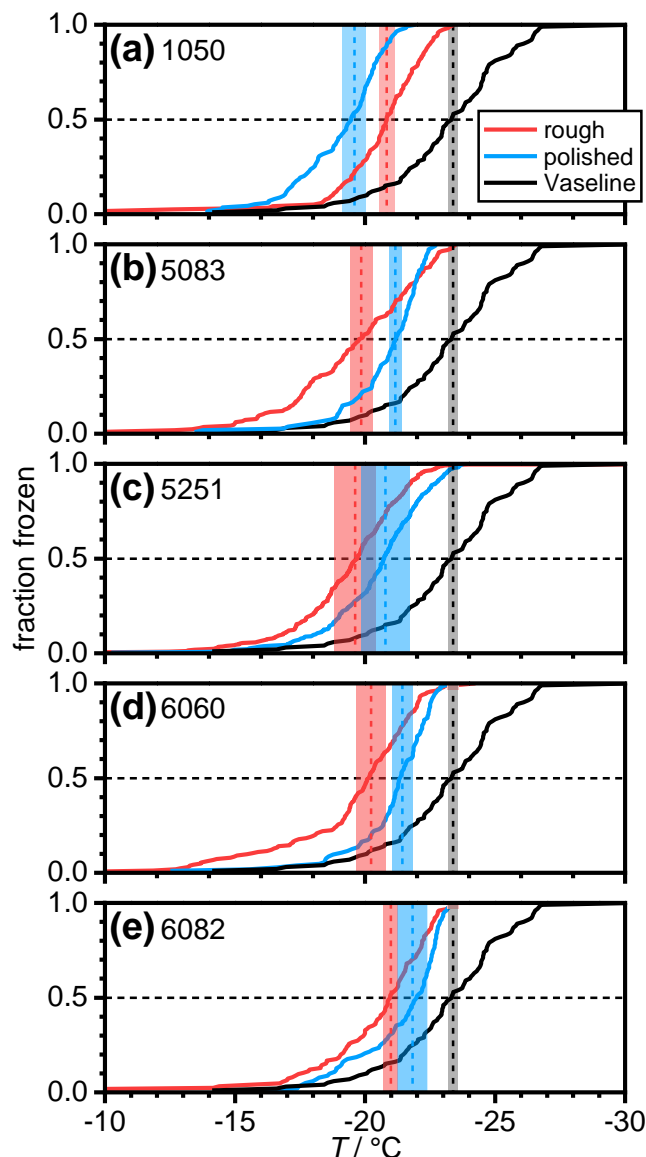


Figure 5. (single column) Fraction-frozen curves recorded upon cooling the various rough (red) and polished (blue) aluminum surfaces at 1°C min^{-1} including the (a) 1050, (b) 5083, (c) 5251, (d) 6060 and (e) 6082 alloys. The fraction frozen curves using Vaseline films are shown as black lines. The $T_{1/2}$ values for the various surfaces are indicated by vertical dashed lines. The shaded regions are estimates of the experimental error of $T_{1/2}$.

All aluminum surfaces display more positive $T_{1/2}$ values compared to the Vaseline experiment indicating that the aluminum surfaces have some ice-nucleating abilities. The largest shift of $T_{1/2}$ from $-23.39 \pm 0.18^\circ\text{C}$ of the Vaseline surfaces to $-19.62 \pm 0.79^\circ\text{C}$ was observed for the rough

5251 surfaces. This means a temperature shift of 3.77 ± 0.81 °C. The trend for the 5083, 5251, 6060, and 6082 alloys is that the $T_{1/2}$ values of the rough surfaces are more positive than the corresponding polished surfaces. This can be attributed to the larger effective surface areas of the rough surfaces and potentially more active ice-nucleation sites, for example, in steep valleys. Computational studies have shown that concave wedge structures in particular with opening angles around 45° can promote ice nucleation.⁴² On the other hand, rough glass, silicon and mica surfaces were found to display very similar ice-properties compared to the corresponding smooth surfaces.⁴⁸ It seems therefore as if the effects of surface roughness on ice nucleation may differ strongly from one material to the next.

Surprisingly, for the 1050 alloy, the $T_{1/2}$ of the polished surface (-19.59 ± 0.45 °C) is more positive than the $T_{1/2}$ of the corresponding rough surface (-20.84 ± 0.3 °C). As mentioned earlier, the polished 1050 surfaces showed more pit structures than the other polished surfaces resulting in a negative S_{sk} value. It therefore seems likely that the higher $T_{1/2}$ value of the polished 1050 surfaces is due to the frequent pit structures.

Apart from the polished 1050 surfaces, it is a curious observation that all the other fraction-frozen curves reach complete crystallization at approximately the $T_{1/2}$ value of the Vaseline surface. This means that the crystallization temperature of the last droplets to freeze on these aluminum surfaces is about the same as the average freezing temperature of water droplets on the nominally inactive Vaseline surface.

Aluminum surfaces are known to quickly self-passivate forming layers of Al_2O_3 . Even with partial pressures of oxygen below 10^{-5} torr, Al_2O_3 layers with thicknesses in the nanometer range were found to form within several hundred seconds.³⁰ The limiting thickness of the Al_2O_3 films is reached quickly at partial pressures of oxygen of 1 torr following the Cabrera Mott kinetic model of low-temperature metal-oxide growth.³¹ Increasing the oxygen partial pressure above 1 torr has been shown to have no additional effect on the film thickness.³¹ The structure of Al_2O_3 formed by surface oxidation of aluminum is typically $\gamma\text{-Al}_2\text{O}_3$.³² Taking these experimental observations into account, all our aluminum surfaces are expected to be completely covered by layers of Al_2O_3 before the ice nucleation experiments are conducted. The thicknesses of the Al_2O_3 layer on aluminum surfaces are typically in the 2 – 4 nm range.^{49, 50}

To investigate the surface compositions of our samples in more detail, the polished surfaces were investigated with laser-induced breakdown spectroscopy (LIBS). Following an intense blast

with a high-energy laser, the elemental composition is determined from the gas-phase atomic emission spectrum.⁵¹ The average elemental compositions from 25 different locations on each of the surfaces are shown in Figure 6. All aluminum surfaces showed the presence of oxygen as expected from the presence of the Al₂O₃ layers. The largest variations with respect to the oxygen content were found within the 5xxx alloys with the 5251 being most oxidized and the 5083 the least. All surfaces of the 5xxx and 6xxx alloys showed magnesium and small amounts of silicon (see Table 1 for nominal bulk compositions). Alloys in the 6xxx series on the other hand contain similar amounts of magnesium and silicon. Our LIBS measurements therefore indicate that magnesium is enriched to a greater extent at the surfaces compared to silicon. The largest percentage of magnesium is found for the 5251 alloy which is also the most oxidized surface. Ignoring the unusual case of the polished 1050 surface, the most positive $T_{1/2}$ values for both the polished and rough surfaces were found for the 5251 alloy. This suggests a correlation between ice-nucleation ability of aluminum surfaces and their oxygen / magnesium contents at the surface.

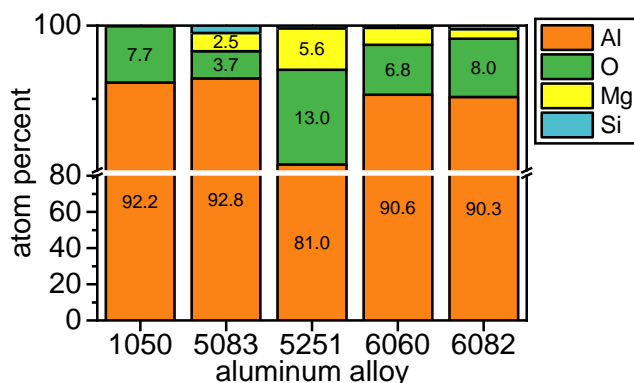


Figure 6. (single column) Atomic composition of the polished surfaces as determined by laser-induced breakdown spectroscopy (LIBS).

In a final step, the effects of surface aging on the ice-nucleation properties of the aluminum surfaces were investigated. Figure 7 shows how $T_{1/2}$ changes as a function of the aging time of the (a) polished and (b) rough surfaces for time periods up to 51 days. At least three freezing experiments were conducted for a given aging time. All surfaces were only used once for a freezing experiment following a given ageing time.

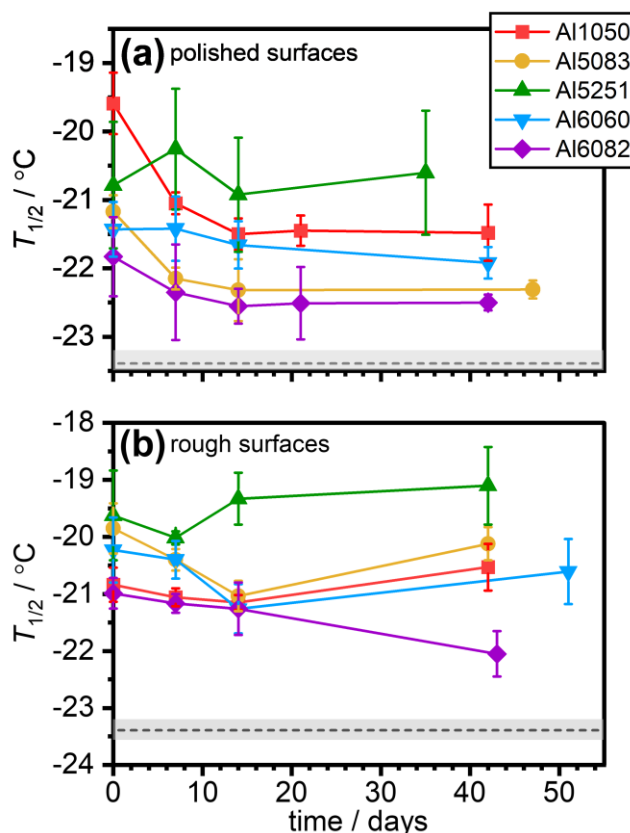


Figure 7. (single column) Effects of surface aging on the ice-nucleation properties of the various aluminum alloys as indicated in the legend with (a) polished and (b) rough surfaces. $T_{1/2}$ reflects the temperature at which half of the droplets were frozen upon cooling at $1\text{ }^{\circ}\text{C min}^{-1}$. The dashed grey lines indicate the $T_{1/2}$ values of water droplets on Vaseline-coated surfaces. The error bars reflect the standard deviations calculated from at least three independent experiments.

Overall, the changes in $T_{1/2}$ as a function of aging time were quite small. For the polished surfaces, statistically significant decreases in $T_{1/2}$ upon aging were observed for the 1050 and 5083 alloys. Interestingly, surface aging removes the unusually high $T_{1/2}$ value of the freshly prepared polished 1050 surfaces. Upon investigating aged 1050 surfaces with optical microscopy, a slightly positive S_{sk} skewness of 0.105 ± 0.560 was obtained. The negative S_{sk} values of the freshly prepared 1050 polished surfaces were earlier attributed to the frequent “pit” features. Surface aging therefore seems to decrease the depths of these features possibly through the formation of thicker Al_2O_3 layers at the bottoms and walls of the pits, and this process could be origin of the decreased ice-nucleation properties. The rough surfaces did not show any statistically significant changes of $T_{1/2}$ upon surface ageing.

The general trend after extended surface aging is that all rough surfaces show more positive $T_{1/2}$ values compared to their polished counterparts. The aged 5251 surfaces are overall the most ice-nucleating surfaces and the aged 6082 surfaces the least.

Conclusions

Aluminum surfaces were found to exhibit moderate ice-nucleation capabilities. An increased degree of surface oxidation and/or higher magnesium content was associated with elevated average ice-nucleation temperatures. In general, rough surfaces promoted ice nucleation more effectively than polished ones. A notable exception was the freshly polished 1050 alloy, the softest aluminum studied, where distinctive pit features, approximately 5 μm in diameter and 1–2 μm deep, appeared to serve as active sites for ice nucleation. Similar nucleating pits have previously been identified on feldspar surfaces.²⁵ Over time, surface aging reduced the activity of these pit features. For the aged surfaces, the 5251 alloy showed the highest ice-nucleation efficiency, while the 6082 alloy exhibited the weakest performance. Future research may focus on deliberately engineering pit structures with optimized dimensions to prolong their activity and enhance ice-nucleation performance.

Supporting Information

Measured and setpoint temperatures upon cooling the sample stage of the IceBox (Fig. S1), and examples of the photographic images taken during cooling of the 7×7 array of water droplets (Fig. S2).

Acknowledgements

We thank Keyence Ltd for access to the LIBS instrument, T. Bernard for help with soldering and C. Ponan for contributions during the early stages of designing the IceBox.

References

- (1) Sellberg, J. A.; Huang, C.; McQueen, T. A.; Loh, N. D.; Laksmono, H.; Schlesinger, D.; Sierra, R. G.; Nordlund, D.; Hampton, C. Y.; Starodub, D.; et al. Ultrafast X-ray probing of water structure below the homogeneous ice nucleation temperature. *Nature* **2014**, *510*, 381–384.

- (2) Xue, H.; Fu, Y.; Lu, Y.; Hao, D.; Li, K.; Bai, G.; Ou-Yang, Z.-C.; Wang, J.; Zhou, X. Spontaneous Freezing of Water between 233 and 235 K Is Not Due to Homogeneous Nucleation. *J. Am. Chem. Soc.* **2021**, *143*, 13548-13556.
- (3) Bai, G.; Gao, D.; Liu, Z.; Zhou, X.; Wang, J. Probing the critical nucleus size for ice formation with graphene oxide nanosheets. *Nature* **2019**, *576*, 437-441.
- (4) Joghataei, M.; Ostovari, F.; Atabakhsh, S.; Tobeiha, N. Heterogeneous Ice Nucleation by Graphene Nanoparticles. *Sci. Rep.* **2020**, *10*, 9723.
- (5) Zhang, S.; Han, J.; Luo, X.; Wang, Z.; Gu, X.; Li, N.; de Souza, N. R.; Garcia Sakai, V.; Chu, X.-Q. Investigations of structural and dynamical mechanisms of ice formation regulated by graphene oxide nanosheets. *Struct. Dyn.* **2021**, *8*, 054901.
- (6) Vonnegut, B. The Nucleation of Ice Formation by Silver Iodide. *J. Appl. Phys.* **1947**, *18*, 593-595.
- (7) Vonnegut, B.; Chessin, H. Ice Nucleation by Coprecipitated Silver Iodide and Silver Bromide. *Science* **1971**, *174*, 945-946.
- (8) Marcolli, C.; Nagare, B.; Welti, A.; Lohmann, U. Ice nucleation efficiency of AgI: review and new insights. *Atmos. Chem. Phys.* **2016**, *16*, 8915-8937.
- (9) Hartmann, S.; Augustin, S.; Clauss, T.; Wex, H.; Šantl-Temkiv, T.; Voigtländer, J.; Niedermeier, D.; Stratmann, F. Immersion freezing of ice nucleation active protein complexes. *Atmos. Chem. Phys.* **2013**, *13*, 5751-5766.
- (10) Polen, M.; Lawlis, E.; Sullivan, R. C. The unstable ice nucleation properties of Snomax® bacterial particles. *J. Geophys. Res. Atmos.* **2016**, *121*, 11,666-611,678.
- (11) Wex, H.; Augustin-Bauditz, S.; Boose, Y.; Budke, C.; Curtius, J.; Diehl, K.; Dreyer, A.; Frank, F.; Hartmann, S.; Hiranuma, N.; et al. Intercomparing different devices for the investigation of ice nucleating particles using Snomax® as test substance. *Atmos. Chem. Phys.* **2015**, *15*, 1463-1485.
- (12) Renzer, G.; de Almeida Ribeiro, I.; Guo, H.-B.; Fröhlich-Nowoisky, J.; Berry, R. J.; Bonn, M.; Molinero, V.; Meister, K. Hierarchical assembly and environmental enhancement of bacterial ice nucleators. *Proc. Natl. Acad. Sci. U.S.A.* **2024**, *121*, e2409283121.
- (13) Knopf, D. A.; Alpert, P. A. Atmospheric ice nucleation. *Nat. Rev. Phys.* **2023**, *5*, 203-217.
- (14) Lukas, M.; Schwidetzky, R.; Eufemio, R. J.; Bonn, M.; Meister, K. Toward Understanding Bacterial Ice Nucleation. *J. Phys. Chem. B* **2022**, *126*, 1861-1867.

- (15) Zhang, Z.; Liu, X.-Y. Control of ice nucleation: freezing and antifreeze strategies. *Chem. Soc. Rev.* **2018**, *47*, 7116-7139.
- (16) Chang, T.; Zhao, G. Ice Inhibition for Cryopreservation: Materials, Strategies, and Challenges. *Adv. Sci.* **2021**, *8*, 2002425.
- (17) Maeda, N. Brief Overview of Ice Nucleation. *Molecules* **2021**, *26*.
- (18) John Morris, G.; Acton, E. Controlled ice nucleation in cryopreservation – A review. *Cryobiology* **2013**, *66*, 85-92.
- (19) Shen, Y.; Wu, X.; Tao, J.; Zhu, C.; Lai, Y.; Chen, Z. Icephobic materials: Fundamentals, performance evaluation, and applications. *Prog. Mater. Sci.* **2019**, *103*, 509-557.
- (20) Fitzner, M.; Sosso, G. C.; Cox, S. J.; Michaelides, A. The Many Faces of Heterogeneous Ice Nucleation: Interplay Between Surface Morphology and Hydrophobicity. *J. Am. Chem. Soc.* **2015**, *137*, 13658-13669.
- (21) Sosso, G. C.; Sudera, P.; Backes, A. T.; Whale, T. F.; Fröhlich-Nowoisky, J.; Bonn, M.; Michaelides, A.; Backus, E. H. G. The role of structural order in heterogeneous ice nucleation. *Chem. Sci.* **2022**, *13*, 5014-5026.
- (22) Davies, M. B.; Fitzner, M.; Michaelides, A. Accurate prediction of ice nucleation from room temperature water. *Proc. Natl. Acad. Sci. U.S.A.* **2022**, *119*, e2205347119.
- (23) Piaggi, P. M.; Weis, J.; Panagiotopoulos, A. Z.; Debenedetti, P. G.; Car, R. Homogeneous ice nucleation in an ab initio machine-learning model of water. *Proc. Natl. Acad. Sci. U.S.A.* **2022**, *119*, e2207294119.
- (24) Kiselev, A.; Bachmann, F.; Pedevilla, P.; Cox, S. J.; Michaelides, A.; Gerthsen, D.; Leisner, T. Active sites in heterogeneous ice nucleation—the example of K-rich feldspars. *Science* **2017**, *355*, 367-371.
- (25) Holden, M. A.; Whale, T. F.; Tarn, M. D.; O’Sullivan, D.; Walshaw, R. D.; Murray, B. J.; Meldrum, F. C.; Christenson, H. K. High-speed imaging of ice nucleation in water proves the existence of active sites. *Sci. Adv.* **2019**, *5*, eaav4316.
- (26) Campbell, J. M.; Meldrum, F. C.; Christenson, H. K. Observing the formation of ice and organic crystals in active sites. *Proc. Natl. Acad. Sci. U.S.A.* **2017**, *114*, 810-815.
- (27) Holden, M. A.; Campbell, J. M.; Meldrum, F. C.; Murray, B. J.; Christenson, H. K. Active sites for ice nucleation differ depending on nucleation mode. *Proc. Natl. Acad. Sci. U.S.A.* **2021**, *118*, e2022859118.

- (28) Coluzza, I.; Creamean, J.; Rossi, M. J.; Wex, H.; Alpert, P. A.; Bianco, V.; Boose, Y.; Dellago, C.; Felgitsch, L.; Fröhlich-Nowoisky, J.; et al. Perspectives on the Future of Ice Nucleation Research: Research Needs and Unanswered Questions Identified from Two International Workshops. In *Atmosphere*, 2017; Vol. 8.
- (29) Properties and Selection: Nonferrous Alloys and Special-Purpose Materials. In *ASM Handbook Volume 2*, Cayless, R., Ed.; ASM International: 1990; Vol. 2.
- (30) Nguyen, L.; Hashimoto, T.; Zakharov, D. N.; Stach, E. A.; Rooney, A. P.; Berkels, B.; Thompson, G. E.; Haigh, S. J.; Burnett, T. L. Atomic-Scale Insights into the Oxidation of Aluminum. *ACS Appl. Mater. Interfaces* **2018**, *10*, 2230-2235.
- (31) Cai, N.; Zhou, G.; Müller, K.; Starr, D. E. Tuning the Limiting Thickness of a Thin Oxide Layer on Al(111) with Oxygen Gas Pressure. *Phys. Rev. Lett.* **2011**, *107*, 035502.
- (32) Raveh, A.; Tsameret, Z. K.; Grossman, E. Surface characterization of thin layers of aluminium oxide. *Surf. Coat. Technol.* **1997**, *88*, 103-111.
- (33) Chong, E.; King, M.; Marak, K. E.; Freedman, M. A. The Effect of Crystallinity and Crystal Structure on the Immersion Freezing of Alumina. *J. Phys. Chem. A* **2019**, *123*, 2447-2456.
- (34) Soni, A.; Patey, G. N. Why α -Alumina Is an Effective Ice Nucleus. *J. Phys. Chem. C* **2019**, *123*, 26424-26431.
- (35) Abdelmonem, A.; Backus, E. H. G.; Hoffmann, N.; Sánchez, M. A.; Cyran, J. D.; Kiselev, A.; Bonn, M. Surface-charge-induced orientation of interfacial water suppresses heterogeneous ice nucleation on α -alumina (0001). *Atmos. Chem. Phys.* **2017**, *17*, 7827-7837.
- (36) Ren, Y.; Soni, A.; Kumar, A.; Bertram, A. K.; Patey, G. N. Effects of pH on Ice Nucleation by the α -Alumina (0001) Surface. *J. Phys. Chem. C* **2022**, *126*, 19934-19946.
- (37) Apelt, S.; Bergmann, U. Icephobicity of aluminium samples is not affected by pH-generated surface charge. *Appl. Surface Sci.* **2023**, *608*, 155039.
- (38) Archuleta, C. M.; DeMott, P. J.; Kreidenweis, S. M. Ice nucleation by surrogates for atmospheric mineral dust and mineral dust/sulfate particles at cirrus temperatures. *Atmos. Chem. Phys.* **2005**, *5*, 2617-2634.
- (39) Menini, R.; Farzaneh, M. Elaboration of Al₂O₃/PTFE icephobic coatings for protecting aluminum surfaces. *Surf. Coat. Technol.* **2009**, *203*, 1941-1946.

- (40) Menini, R.; Ghalmi, Z.; Farzaneh, M. Highly resistant icephobic coatings on aluminum alloys. *Cold Reg.Sci. Technol.* **2011**, *65*, 65-69.
- (41) Zhang, Y.; Ge, D.; Yang, S. Spray-coating of superhydrophobic aluminum alloys with enhanced mechanical robustness. *J. Colloid Interf. Sci.* **2014**, *423*, 101-107.
- (42) Bi, Y.; Cao, B.; Li, T. Enhanced heterogeneous ice nucleation by special surface geometry. *Nat. Comm.* **2017**, *8*, 15372.
- (43) Graeber, G.; Schutzius, T. M.; Eghlidi, H.; Poulikakos, D. Spontaneous self-dislodging of freezing water droplets and the role of wettability. *Proc. Natl. Acad. Sci. USA* **2017**, *114*, 11040-11045.
- (44) Whale, T. F.; Murray, B. J.; O'Sullivan, D.; Wilson, T. W.; Umo, N. S.; Baustian, K. J.; Atkinson, J. D.; Workneh, D. A.; Morris, G. J. A technique for quantifying heterogeneous ice nucleation in microlitre supercooled water droplets. *Atmos. Meas. Tech.* **2015**, *8*, 2437-2447.
- (45) Tobo, Y. An improved approach for measuring immersion freezing in large droplets over a wide temperature range. *Sci. Rep.* **2016**, *6*, 32930.
- (46) Ganguly, M.; Dib, S.; Ariya, P. A. Purely Inorganic Highly Efficient Ice Nucleating Particle. *ACS Omega* **2018**, *3*, 3384-3395.
- (47) Pereira Freitas, G.; Adachi, K.; Conen, F.; Heslin-Rees, D.; Krejci, R.; Tobo, Y.; Yttri, K. E.; Zieger, P. Regionally sourced bioaerosols drive high-temperature ice nucleating particles in the Arctic. *Nat. Comm.* **2023**, *14*, 5997.
- (48) Campbell, J. M.; Meldrum, F. C.; Christenson, H. K. Is Ice Nucleation from Supercooled Water Insensitive to Surface Roughness? *J. Phys. Chem. C* **2015**, *119*, 1164-1169.
- (49) Cornette, P.; Zanna, S.; Seyeux, A.; Costa, D.; Marcus, P. The native oxide film on a model aluminium-copper alloy studied by XPS and ToF-SIMS. *Corros. Sci.* **2020**, *174*, 108837.
- (50) Olefjord, I.; Mathieu, H. J.; Marcus, P. Intercomparison of surface analysis of thin aluminium oxide films. *Surf. Interface Anal.* **1990**, *15*, 681-692.
- (51) Hussain Shah, S. K.; Iqbal, J.; Ahmad, P.; Khandaker, M. U.; Haq, S.; Naeem, M. Laser induced breakdown spectroscopy methods and applications: A comprehensive review. *Radiat. Phys. Chem.* **2020**, *170*, 108666.

Table of Contents image

